Local Binary Pattern and RVFL for Covid-19 Diagnosis

Mengke Wang(✉)

School of Computer Science and Technology, Henan Polytechnic University, Jiaozuo 454000, Henan, People's Republic of China
mengkewang@home.hpu.edu.cn

Abstract. Recently, the use of artificial intelligence to improve the efficiency of Covid-19 diagnosis has become a trend due to the spread and proliferation of Covid-19 and the fact that healthcare professionals alone are no longer sufficient to cope with the rapid spread of Covid-19. Chest computed tomography (CT) is an effective method to diagnose Covid-19. Using image processing methods to help diagnose such images has become critical. In this trend, we propose a way to detect Covid-19 efficiently. The scheme employs a hybrid model. Local binary patterns (LBP) implement feature extraction in the preprocessing stage. Validation classification results are obtained using the random vector functional link (RVFL) network, which is finally validated by 10-fold cross-validation. It experimentally demonstrated the usefulness of our proposed model for diagnostic-level progress. It helps healthcare workers accurately identify Covid-19.

Keywords: local binary pattern · random vector functional link network · deep residual network · Covid-19

1 Introduction

1.1 Background

Covid-19 spread rapidly around the world from the moment it was discovered in December 2019, and as of mid-May 2022, there have been hundreds of millions of patients with Covid-19, and many people died of the disease worldwide [1, 2]. Covid-19 has not wholly disappeared, and confirmed cases continue to rise, severely impacting our lives [3]. Covid-19 can form acute respiratory syndromes and spread rapidly around the world. The virus is called coronavirus due to its appearance of spike-like structures [4]. Most people with Covid-19 present with fever, sore throat, and general discomfort and need rest to recover [5, 6]. However, some patients have more severe conditions, exceptionally the orderly, which can be life-threatening [7, 8]. It can be life-threatening in extreme cases. Therefore, to avoid unnecessary deaths. We need timely diagnosis and treatment [9]. During an outbreak, real-time reverse transcription polymerase chain reaction (RT-PCR) is used to diagnose Covid-19.

B. Wang et al. (Eds.): ICMTEL 2023, LNICST 532, pp. 325–343, 2024.
https://doi.org/10.1007/978-3-031-50571-3_23

However, the diagnosis of a suspected patient can only be made if the test is positive. This method cannot exclude the interference of other factors, and it takes time. So, it is urgent to present one machine learning model to detect this disease automatically [10, 11], and we need to apply the computer vision aspect of seeing Covid-19 to clinical practice. Machine learning models have long provided treatment and assistance for many diseases and are much more efficient than manual ones [12]. For example, there are machine learning models that make it easier for people with visual impairments and make life easier for patients [13]. The machine learning model can be an excellent alternative to RT-PCR to diagnose the early stages of Covid-19 [14]. Our imaging device, chest CT, would be beneficial in diagnosing Covid-19 [15]. The continuous development of computer science over the years has added to the field of medical imaging. Machine learning and deep learning are increasingly important in medical image processing. Support vector machines (SVM) [16] also perform well in predicting disease types.

However, the main problem with deep learning is using back propagation (BP) methods to tune the parameters, which have many drawbacks. For example, the BP algorithm is a gradient descent algorithm, and the objective function that needs to be optimized is very complex, leading to the inefficiency of the BP algorithm and the convergence rate of the network becoming slow. In addition, the network weights of the BP algorithm can fail to train if they are reoriented. Its initial weights are too sensitive, leading to different results for each training. And there is instability in its learning rate. So, to improve these drawbacks, this paper uses a feedforward neural network RVFL to classify CT images. LBP is used to extract the texture features of CT images.

1.2 Related Work

Nowadays, deep learning is becoming more and more potent as it is widely used in various aspects. We can use this technology to solve Covid-19 diagnostic problems. Since 2020, the worst catastrophe facing humanity is Covid-19. Therefore, we should conduct research on Covid-19 in all possible places. At the same time, deep learning researchers have also begun to use all possible methods. Through computer-assisted Covid-19, they can help medical workers.

Ismael and Sengur [17] used three methods to identify and classify the Covid-19 virus on chest X-ray (CXR) images. And all three ways achieved good accuracy, sensitivity, and specificity. Jain et al. [18] extract 6432 CXR from the Kaggle repository scanning sample, compare the three models, and report their accuracy. Similarly, he evaluates the model regarding accuracy, sensitivity, and specificity. He also pointed out that the high precision may result from over-fitting. Aminu et al. [19] proposed a new deep learning model, but the model has few parameters, and if the number of trained data is large, then training cannot be performed. The authors use the L2 regularization method merged with the global average to avoid new problems due to insufficient data. The technique works by extracting Covid-Net models and providing them to various classifiers that measure the model's effectiveness. A hybrid model was presented by Zhang et al. [20]. They used wavelet and the three-stage biogeography-based optimization (3SBBO) method for feature extraction, and updating of weights and biases. A cross-validation method was also used to obtain more accurate results. Two models of CNN named Covid-RNet-1 and Covid-RENet-2 were proposed by Khan et al. [21]. The authors used CNN architecture

for convolutional operations to classify images in the dataset and obtained high scores in terms of accuracy, MCC and F1 [22].

1.2.1 WE-ABC

Wavelet entropy and artificial bee colony (WE-ABC) algorithms use WE for feature extraction of CT images and then combine the advantages of the ABC algorithm with few parameters and simple computation to find the most suitable solution to the problem and verify Covid-19. It is well known that the Fourier transform is used to transform signals. The signal after the Fourier transform is decomposed into its constituent frequencies by the Fourier transform. And the altered function has the form of different combinations of sine waves [10].

However, the Fourier transform also has some drawbacks. For example, if accurate localization in the time domain is required, all signals in the corresponding frequency domain must be analyzed. Since wavelet transform has more variables, wavelet transform is used instead of Fourier transform. If a denotes scale, τ represents translation, ψ is wavelet, and m stands for time. Then, the formula is as follows:

$$L(a, \tau) = \frac{1}{\sqrt{a}} \int_{-\infty}^{\infty} f(m)\psi\left(\frac{m-\tau}{a}\right)dm \tag{1}$$

The ABC algorithm is an optimization method. By simulating the nectar collection mechanism of actual bees, the bees in the algorithm are classified into three types: honey-gathering bees, observation bees, and scout bees. The three species of bees have different jobs, but they can be interchanged under certain conditions, as shown in Fig. 1:

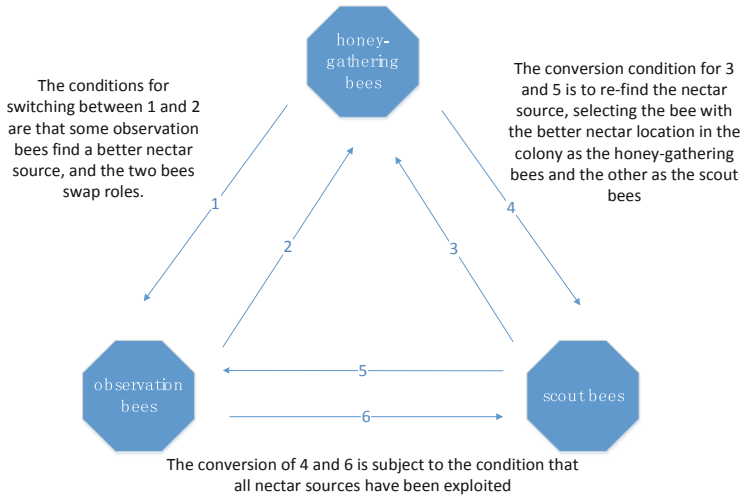

Fig. 1. Interconversion diagram of three species of bees.

In the initialization formula of the ABC algorithm, x_m represents a feasible method, with n variables in each viable strategy. We assume that the number of bees collected

and observed is N, so the value of m is from 1 to N, and the value of i is from 1 to n.

$$x_{mi} = l_i + \text{rand}(0, 1) \times (u_i - l_i) \tag{2}$$

The u_i and l_i represent the maximum and minimum boundaries of x_{mi}, respectively.

Each hired bee searches for nearby feasible solutions by some already existing feasible solutions. Then, selected by a greedy algorithm. Use f_m as the target function of x_m. The formula is as follows:

$$\text{fit}_{m(X_m)} = \begin{cases} \frac{1}{1+f_{m(x_m)}} & \text{if } f_{m(x_m)} \geq 0 \\ 1 + \text{abs}(f_{m(x_m)}) & \text{if } f_{m(x_m)} < 0 \end{cases} \tag{3}$$

The scout bee judges the viable solution brought back by the hired bee to be available. If this viable solution is still not optimized after several updates, it will move on to the next new viable solution. The probability formula for food source selection is:

$$P_m = \frac{\text{fit}_{m(x_m)}}{\sum_{m=1}^{N} \text{fit}_{m(x_m)}} \tag{4}$$

1.2.2 GLCM-GA

Gray-level cooccurrence matrix and genetic algorithm (GLCM-GA) is a hybrid construction of GLCM and GA [23]. In which GLCM performs the extraction of image features, and the GLCM-GA model is optimized using GA. Finally, the experimental results are obtained using the feedforward neural network classification function. If two pixels in an image have their orientation and the distance between them already specified between them. Then their spatial relationship can be calculated using GLCM. The features of the image texture are represented using image greyscale. The GLCM reacts to the spatially relevant features of an image using four features: energy, entropy, contrast, and homogeneity.

The GA algorithm mimics the Darwinian evolutionary selection process by necessity and is essentially an efficient, global search method. As the algorithm is trained, it can gain more and more valid information during the search process and apply this valuable information to the following algorithm. The algorithm becomes more and more efficient by accumulating search information in this way. The algorithm consists of five main steps: image initialization, three operations, and termination condition determination. As shown in Fig. 2 m refers to the evolutionary algebraic calculator.

1.2.3 WE-ELM

The most important feature of the extreme learning machine (ELM) is that it learns more efficiently than traditional learning algorithms, such as single-layer feedforward neural networks (SLFN). It is also more accurate and stable. The overall structure of ELM comprises an input layer, a hidden layer, and an output layer. Each of these three layers is composed of one or more neurons. ELM is unidirectional because it satisfies a one-way propagation process. Each neuron is the output of the last neuron and the input

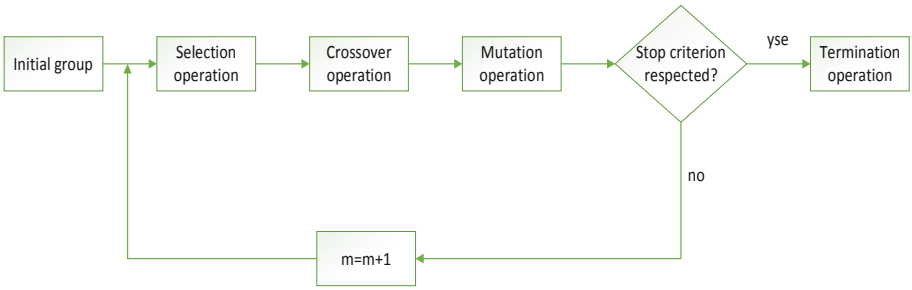

Fig. 2. Diagram of a genetic algorithm.

of the next neuron [24]. A standard SLFN structure is shown in Fig. 3. In the figure, w is the connection weight between the input layer and the implied layer, k is the output layer weight, x_n denotes the data example, y_m means the token corresponding to the data example, and the middle O_i means the implied layer.

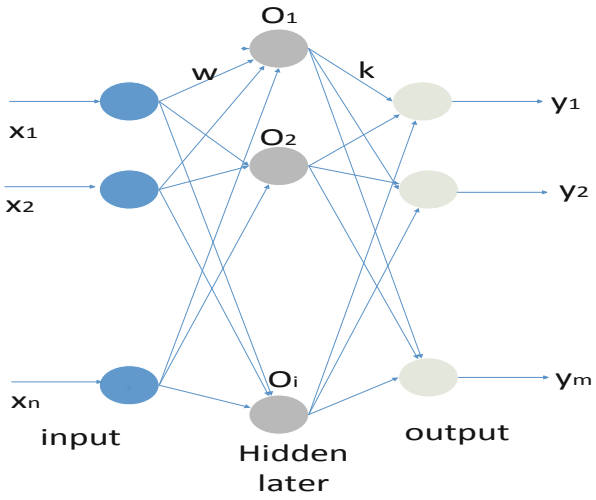

Fig. 3. Single hidden layer neural network structure.

The network structure of the EL model is the same as that of SLFN, except that instead of the traditional gradient-based algorithm that has been tried and tested in neural networks, random input layer weights, and deviations are used in the training phase. The ELM training SLFN consists of stochastic feature mapping and a linear parameter solution.

1.3 Deep Residual Network

The deep residual learning structure solves the degradation problem of network models. Image recognition techniques using this model can improve their recognition performance [25]. It is implemented by having the intermediate stack network layer explicitly fit a residual mapping rather than having these residual network structures fit a desired potential mapping relationship. It is not connected directly but is a residual mapping of the network computation [26]. Therefore, in the network structure, there is no direct connection between the weights of this layer and the weights of its upper layers, causing it to incur a convergence delay [27]. In the residual network, each residual block extracts valuable features. This simplified network training. Figure 4 shows the general process of the residual structure. The activation function x consists of convolution, pooling, stepping, and get (x). It is mapped from the previous layer of the network and obtained by varying it. Adding the activation function x to the transformed H(x), H(x) + x is the resultant vector. Each block optimizes the activation function by this method and retains the parameters of the original activation function x [28].

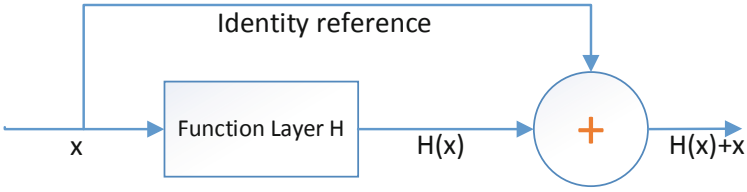

Fig. 4. Residual block.

1.4 Our Work

Usually, when training neural networks, the forward neural network training speed is slow. This paper proposes a model combining RVFL and LBP for better diagnosis. First, feature extraction is performed using LBP, then classification results are obtained using RVFL. Using the hybrid network model can improve the accuracy of diagnosis, and the time of diagnosis is also shortened. RVFL has a significant speed advantage for the same learning content as it takes a much shorter time to learn than the traditional forward neural network. Therefore, the model in this paper can diagnose lung images more quickly and efficiently, which is beneficial to disease control and contributes to Covid-19.

2 Dataset

In this research work, the CT configuration and image acquisition is performed as follows: Philips Ingenuity 64-row spiral CT machine, MAS is 240, KV is 120, its layer thickness is 3 mm, layer pitch is also 3 mm, the pitch is 1.5: the width of the lung window is 1500 HU, the length of the lung window is 500 HU, the width of the mediastinal

window is 350 HU, the length of the lung window is 60 HU, and then the lesions are reconstructed by taking images of the lungs. The lung window image is generated with a layer thickness of 1 mm, and the generated layer spacing is also 1 mm. The person being examined will need to lie on their back, stop breathing and then take a deep breath for a routine scan from the tip of their lungs to the angle of their rib diaphragm.

The hierarchical selection method is used for each subject in the experiment to select between 1 and 4 slice sections. The stratified selection method is used for those with Covid-19, but there are no restrictions for those without the disease, and any image level can be selected. The resolution of all images used in the experiment was 1024×1024. When two results have different (J_1, J_2) arise, a higher-level physician (β) needs to be asked to share the same view. Suppose X refers to the CCT image scan and N is the label of each expert and the $\overline{N}$ the following equation can find the label:

$$\overline{N}(X) = \begin{cases} N(J_1) & N(J_1) = N(J_2) \\ NV(N_{all}) & \text{else} \end{cases} \tag{5}$$

$$N_{all} = [N(J)_1, N(J_2), N(\beta)] \tag{6}$$

where NV indicates a majority vote, N_{all} stands for All Experts label.

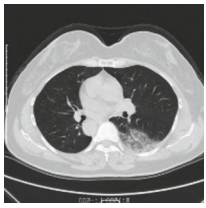

Fig. 5. A unprocessed Covid-19 image.

Figure 5 shows the Covid-19 unprocessed image. After preprocessing operations on the image (image scaling and normalization), feature extraction is performed on CCT medical images. By image features, we mean the semantic image information contained in an image, for example, brightness, edges, texture, and colors. It is obtained by transforming the image. Feature extraction can reduce the dimensionality and complexity of an image without losing the image information, which is beneficial to image processing. In this paper, we use the LBP algorithm to extract some desired features from the chest image dataset of Covid-19.

Figure 6 is a flowchart which image processing. In the preprocessing stage, grayscale images are obtained, followed by histogram pull and then cropping out the text at the edges of the images to get the cropped dataset after cropping. Finally, an image needs to be sampled twice to become of size $[256 \times 256]$ (There are four variables for cropping during the set of the values of TOP, BOOT, LEFT, and RIGHT to 150). This operation can save us a lot of hardware resources.

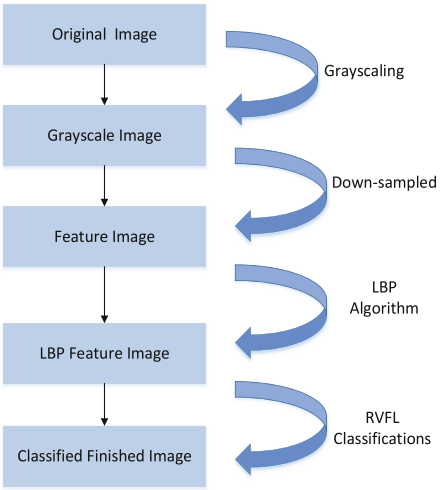

Fig. 6. Preprocessing.

3 Methodology

3.1 LBP

LBP is a feature extractor often used to extract features [4]. It is a traditional texture analysis descriptor that has received attention in the last decade. LBP is robust to some properties, such as invariance to illumination panning and scaling, achieving state-of-the-art results in some applications. For example, in the face recognition system, LBP texture characteristics are used as the input of deep networks, the network parameters are obtained through the greedy training network layer by layer, and the test sample is predicted with a trained network [29, 30]. Compared with the characteristic face method, the recognition rate of LBP has dramatically improved.

When the LBP algorithm was first proposed, it was defined in a 3×3 pixel neighborhood. The LBP algorithm is described as follows: We must select a pixel point as the central pixel point and take its value as the threshold. Then the neighboring pixel values around it and the center pixel value are compared individually. If it is higher than the central pixel value, it is marked as 1; if it is lower than the central pixel value, it is marked as 0. By this method, the pixel value is described by LBP. LBP value reflects the texture characteristics of this image block. The following Fig. 7 shows:

To define it, use a more standard formula.

$$L(x_c, y_c) = \sum_{p=0}^{p-1} 2^p s(i_p - i_c) \tag{7}$$

where (x_c, y_c) represent the middle elements, its value is i_c, and peripheral pixel value is i_p. The symbolic function $s(x)$ is represented as follows:

$$s(x) = \begin{cases} 1 & x \geq 0 \\ 0 & x < 0 \end{cases} \tag{8}$$

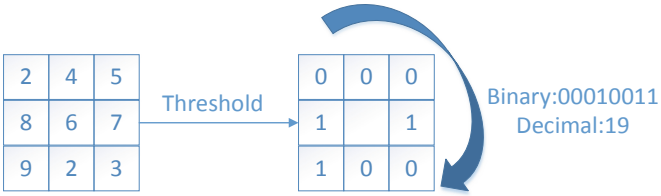

Fig. 7. Principle of the LBP.

The initial algorithm covers only the regions with previously specified radii. Still, the LBP algorithm does not work if it is not a region with a fixed radius size. So, to extract texture features of different radii, grayscale, and rotation invariance are achieved. The domain of the improved LBP algorithm is extended to an arbitrary neighborhood, and the shape of the field becomes circular [31]. The optimized LBP algorithm specifies a random number of pixel points in a neighborhood of radius R [32]. The equation computes the value of the sampling point:

$$x_p = x_c + R\cos\left(\frac{2\pi p}{P}\right) \tag{9}$$

$$y_p = y_c - R\sin\left(\frac{2\pi p}{P}\right) \tag{10}$$

(x_p, y_p), $p \in P$ is a certain pixel point. The coordinates of the calculated sample points may not be exact integers, and the computational procedure for using bilinear interpolation to find the pixel values of an image is shown below:

$$f(x, y) \approx \begin{bmatrix} 1 - x & x \end{bmatrix} \begin{bmatrix} f(0,0) & f(0,1) \\ f(1,0) & f(1,1) \end{bmatrix} \begin{bmatrix} 1 - y \\ y \end{bmatrix} \tag{11}$$

If the region to be sampled is a region of radius R, the LBP algorithm can turn P sampling points into 2^P patterns. It can be seen that if the number of sampling points increases, the variety of binary patterns also increases sharply. For example, in a 5×5 neighborhood, there are $2^{20} = 1048576$ binary modes. But more binary patterns are not better. Too many binary patterns are not suitable for texture feature extraction. So, it is vital to use less amount of data to achieve an optimal representation. Make it get fully utilized.

To overcome the above problems and further improve the performance of the LBP algorithm, Ojala et al. [33] presented an "equivalent pattern" to decrease the pattern type of the LBP operator. If the cyclic binary numbers have at most two transformations from 0 to 1 or 1 to 0, these are called equivalent pattern classes. The following Fig. 8 shows schematic diagrams of several equivalent patterns:

This way, the number of modes is reduced to $P(P - 1) + 2$, and the dimensionality of the feature vector is reduced. At the same time, the effect of high-frequency noise generation is reduced.

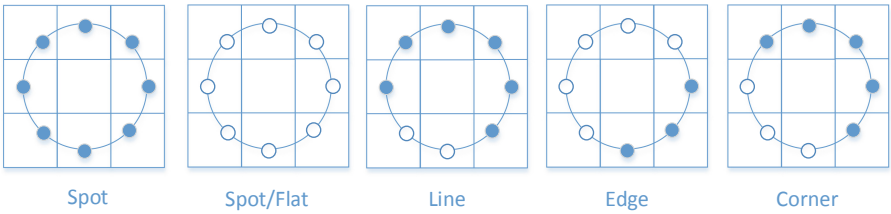

Fig. 8. Equivalent patterns.

3.2 RVFL

RVFL is presented by Zhang and Yang [34]. It is a single hidden layer neural network. It is a special kind of network. The ELM [35, 36] is a commonly used non-iterative learning model, but RVFL works better [37]. The difference between RVFL and ELM model structures are similar and different, where Fig. 9 is the RVFL model, and Fig. 10 is the ELM model. The green line in the figure represents a direct connection between the input and output layers. The blue line weights do not need to be calculated. They are generated randomly. The letter H in the figure denotes the features of the hidden layer, X marks our input features, S is the input weight of the RVFL framework, and E is the input weight of the ELM framework. Moreover, once generated, they do not change. But the output weights need to be computed.

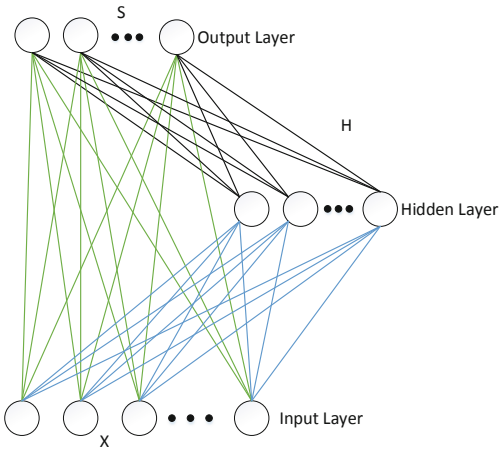

Fig. 9. Framework of RVFL networks.

In addition to the traditional BP-trained neural networks, randomization-based neural networks are also gaining attention. This kind of neural network can solve the defects of closed neural networks. It does not have the disadvantages of traditional neural networks: more efficient training and better learning ability than conventional neural networks [38]. RVFL is rapidly gaining great appeal due to its excellent performance in different fields, such as visual tracking, classification regression, and prediction. The original features

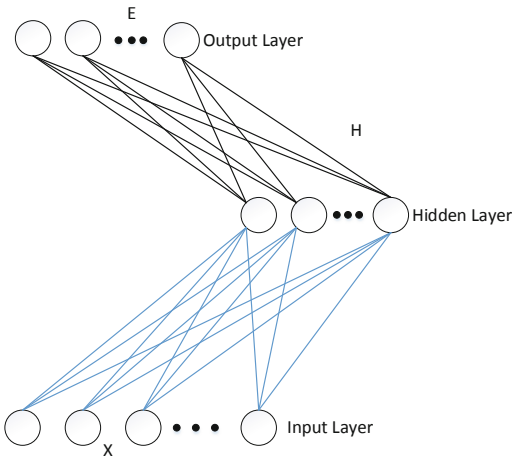

Fig. 10. Framework ELM networks.

of RVFL are reused and can also be propagated to the output layer by direct links. The RVFL network is thinner, simpler, and more attractive than others.

In addition, unlike deep neural networks, RVFL neural networks (RVFLNN) are equivalent to placing the hidden layer directly into the input layer as an enhancement node. The RVFLNN performs a nonlinear change of the input vector right at the input. Since RVFLNN is a concise planar network structure, RVFLNN is faster in supervised learning and training with good generalization performance. It uses fewer samples for training, and the network can achieve the required accuracy in a given dataset region. RVFLNN improves the generalization performance by augmenting the nonlinear kernel raw data with implicit layer learning [39].

3.3 K-Fold Cross-Validation

After classifying the model, we need to evaluate the classifier's performance statistics. In this paper, we use cross-validation to accomplish this task. Typically, we divide the raw data into two categories, a training set, and a test set. Finally, the validation set is used to test the performance metrics of the trained model [40, 41]. The K-fold cross-validation method divides the dataset into K subsets, with each subset of data doing a separate validation set and the remaining $K - 1$ sets of subset data serving as the training set to obtain K models. We take the 10-fold cross-validation method as an example to illustrate the specific steps of the K-fold cross-validation method. First, all the data sets are divided into ten equal parts, and the ten cross-validation sets are numbered 1, 2, 3, 4, 5, 6, 7, 8, 9, and 10. And then, set number one is taken as the validation set, the remaining nine sets are taken as the training set, and the remaining nine sets are taken as a validation set in turn [42]. As shown in Fig. 11, the errors were summed and averaged to obtain the cross-validation errors [43]. E_i in the graph is the test result error, with values of i ranging from 1 to 10. E is the average of these ten errors.

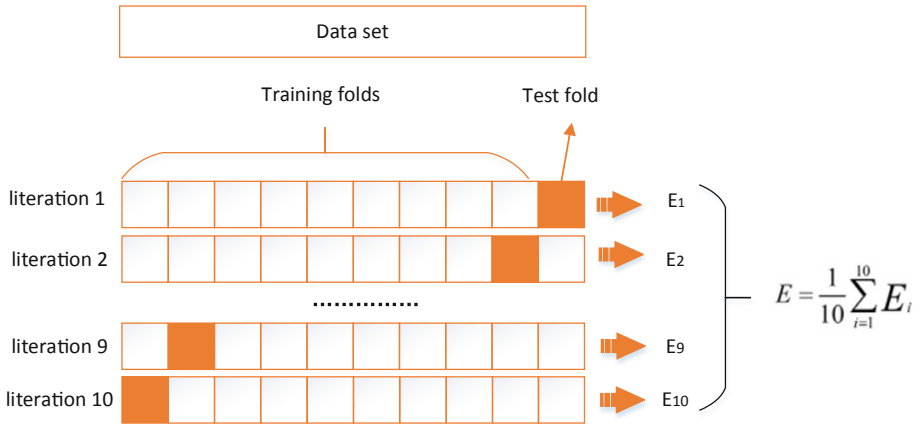

Fig. 11. 10-fold cross-validation.

K-fold cross-validation effectively avoids problems such as over-learning and under-learning, as well as a method to evaluate machine learning models. It judges the effectiveness of models by obtaining the highest accuracy and consistency of various regression models. The K-fold cross-validation method helps us to select the appropriate model and is widely used to enumerate the relative efficiency of multiple models.

3.4 Measurement

Classification is a core issue in supervised learning. In this paper, the detection of Covid-19 is a dichotomous problem. To determine how well a classifier classifies, we usually use a confusion matrix to assess the classifier's performance. We need to introduce some performance evaluation indicators of dichotomous problems, and some commonly used metrics include sensitivity, specificity, precision, accuracy, MCC, F1, FMI, etc.

In machine learning, especially statistical classification problems, the confusion matrix exists in a tabular layout, as shown in Table 1 The confusion matrix visualizes the algorithm's performance and allows us to see the categories. The dichotomous confusion matrix we use includes four types. Where TP and TN represent the number of samples where the predicted value is the same as the actual value, FN and FP represent the number of samples where the predicted value is the opposite of the actual value, and the prediction is wrong.

Table 1. Confusion matrix

	True Value = 1	Predicted value = 0
True Value = 1	TP	FN
Predicted value = 0	FP	TN

Below are details of the seven judgment criteria used to measure the model's performance.

(1) Sensitivity

Sensitivity is the probability of correctly detecting a disease. In medical testing, the sensitivity of a test (sometimes referred to clinically as the detection rate) is the ratio of people who are detected as having the disease to those who have it. The calculation formula can be expressed as follows:

$$\text{sensitivity} = \frac{\text{TP}}{\text{TP} + \text{FN}} \times 100\% \tag{12}$$

(2) Specificity

Consider examples of medical tests used to diagnose diseases. The specificity of a test is the percentage of people who are ill but have a negative test result. The calculation formula can be expressed as follows:

$$\text{specificity} = \frac{\text{TN}}{\text{TN} + \text{FP}} \times 100\% \tag{13}$$

A positive result indicates a high probability of disease. However, a negative test does not necessarily help rule out disease.

(3) Precision

Precision is the number of samples that can be correctly identified as diseased by the classifier among the truly diseased samples. The formula for calculating this is as follows:

$$\text{Precision} = \frac{\text{TP}}{\text{TP} + \text{FP}} \times 100\% \tag{14}$$

(4) Accuracy

Accuracy is the number of samples correctly classified by the classifier in all data and reflects the ability of the classifier to determine the whole sample, that is, to determine the positive ones as positive and the negative ones as negative [44]. The calculation formula can be expressed as follows:

$$\text{accuracy} = \frac{\text{TP} + \text{FN}}{\text{TP} + \text{FN} + \text{TN} + \text{FP}} \times 100\% \tag{15}$$

(5) MCC

The MCC is a particular case of the phi coefficient (φ)[45]. That is, it calculates the True Class and Predicted Class correlation coefficients. The calculation formula can be expressed as follows:

$$\text{MCC} = \frac{\text{TP} \times \text{TN} - \text{FP} \times \text{FN}}{\sqrt{(\text{TP} + \text{FP})(\text{TP} + \text{FN})(\text{TN} + \text{FP})(\text{TN} + \text{FN})}} \times 100\% \tag{16}$$

From the formula, if FP = FN = 0, it indicates a perfect positive correlation. On the contrary, it means an utterly negative correlation. Therefore, the value of MCC is between −1 and 1, while 0 implies that the classifier is not better than random binary selection.

(6) F1

The F-score is the summed mean of precision and recall and is calculated as follows:

$$F_\beta = \left(1+\beta^2\right)\frac{\text{Precision} \times \text{Recall}}{\beta^2 \times \text{Precision} + \text{Recall}} = \left(1+\beta^2\right)\frac{\left(1+\beta^2\right)\text{TP}}{\left(1+\beta^2\right)\text{TP} + \beta^2\text{FP} + \text{FN}} \quad (17)$$

Normally, β takes the value of 1. When β = 1, it is the commonly used F1 value, indicating that precision and recall are as important as each other, and is calculated as follows:

$$\text{F1} = \frac{2\text{TP}}{2\text{TP} + \text{FP} + \text{FN}} \times 100\% \quad (18)$$

The F1 value is also called Balanced F-Score [46, 47]. If the accuracy and recall are high, the F1 value will increase.

(7) FMI

Fowlkes-Mallows index (FMI) is the geometric mean of two-by-two precision and recall [48].

$$\text{FMI} = \frac{\text{TP}}{\sqrt{(\text{TP}+\text{FP})(\text{TP}+\text{FN})}} \times 100\% \quad (19)$$

4 Experiment Result and Discussions

4.1 Statistical Result

The method based on LBP and RVFL aims to detect the chest virus infection caused by Covid-19. In this experiment, 320 lung images were used, including 160 images of Covid-19 and 160 images of normal lungs. The image dataset is preprocessed before training the model. The first step is to set the height and width of all images to 1024 and convert the original images into greyscale images for convolutional pooling operation. Then LBP extracts the processed image features. Finally, the image texture features are classified and judged using RVFL to obtain the classification results. Table 2 shows the data of this model run ten times, indicating that the sensitivity, specificity, precision, accuracy, F1, MCC, and FMI are 77.22 ± 2.33%, 80.53 ± 1.68%, 79.89 ± 1.08%, 78.88 ± 0.79%, 78.51 ± 1.06%, 57.82 ± 1.54%, and 78.53 ± 1.03%, respectively. Figure 12 is the folding point chart of the model's sensitivity, specificity, precision, accuracy, F1, MCC, and FMI.

Table 2. Statistics of experimental results

Run	Sen	Spc	Prc	Acc	F1	MCC	FMI
1	75.94	81.25	80.20	78.59	78.01	57.27	78.04
2	77.50	79.69	79.23	78.59	78.36	57.20	78.36
3	80.62	78.12	78.66	79.38	79.63	58.77	79.64
4	77.19	81.56	80.72	79.38	78.91	58.81	78.93
5	79.06	80.94	80.57	80.00	79.81	60.01	79.81
6	76.88	78.75	78.34	77.81	77.60	55.63	77.61
7	79.06	78.44	78.57	78.75	78.82	57.50	78.82
8	75.00	81.88	80.54	78.44	77.67	57.01	77.72
9	72.50	83.12	81.12	77.81	76.57	55.94	76.69
10	78.44	81.56	80.97	80.00	79.68	60.03	79.69
MSD	77.22 ± 2.33	80.53 ± 1.68	79.89 ± 1.08	78.88 ± 0.79	78.51 ± 1.06	57.82 ± 1.54	78.53 ± 1.03

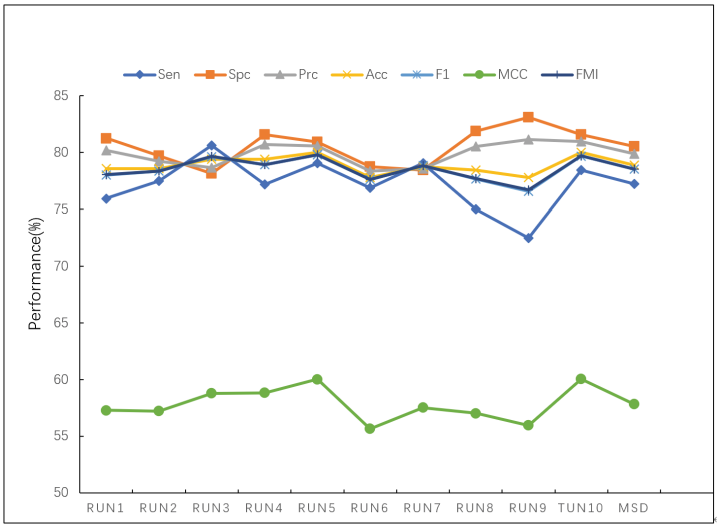

Fig. 12. Performance trends of the LBP-RVFL model.

4.2 Comparison to State-of-the-Art Approaches

To test the feasibility of our proposed model, we validated it using a 10-fold cross-validation method. Then we compared the LBP-RVFL model with three advanced methods: WE-ABC, GLCM-GA, and WE-ELM. As shown in Table 3 and Fig. 13, the best is LBP-RVFL (ours) in terms of sensitivity, specificity, precision, accuracy, MCC, F1, and FMI for detecting Covid-19. Regarding sensitivity, our model is 77.22%, WE-ABC

is 75.14%, GLCM-GA is 74.26%, and WE-ELM is 75.54%. Regarding specificity, our model is 80.53%, WE-ABC is 77.30%, GLCM-GA is 72.30%, and WE-ELM is 77.77%. Regarding precision, our model is 79.89%, WE-ABC is 76.85%, GLCM-GA is 73.28%, and WE-ELM is 76.66%. Regarding accuracy, our model is 78.88%, WE-ABC is 76.22%, GLCM-GA is 73.28%, and WE-ELM is 76.66%. For MCC, our model is 57.82%, WE-ABC is 52.48%, GLCM-GA is 46.63%, and WE-ELM is 53.35%. For F1, our model is 78.51%, WE-ABC is 75.95%, GLCM-GA is 73.50%, and WE-ELM is 76.38%. Regarding FMI, our model is 78.53%, WE-ABC is 75.97%, GLCM-GA is 73.53%, and WE-ELM is 76.39%. Through the above analysis, we found that our proposed LBP-RVFL method performed well in all aspects of Covid-19. Moreover, our model is more stable. Model stability is essential for the diagnosis of diseases. It facilitates the further treatment of the disease.

Table 3. Comparison with state-of-the-art methods for detecting Covid-19

Method	Sen	Spc	Prc	Acc	F1	MCC	FMI
WE-ABC	75.14 ± 1.93	77.30 ± 2.45	76.85 ± 1.72	76.22 ± 0.96	75.95 ± 0.95	52.48 ± 1.95	75.97 ± 0.95
GLCM-GA	74.26 ± 3.60	72.30 ± 2.40	72.86 ± 1.09	73.28 ± 1.07	73.50 ± 1.65	46.63 ± 2.15	73.53 ± 1.65
WE-ELM	75.54 ± 2.54	77.77 ± 1.51	77.27 ± 1.04	76.66 ± 1.14	76.38 ± 1.42	53.35 ± 2.26	76.39 ± 1.41
LBP-RVFL (Ours)	77.22 ± 2.33	80.53 ± 1.68	79.89 ± 1.08	78.88 ± 0.79	78.51 ± 1.06	57.82 ± 1.54	78.53 ± 1.03

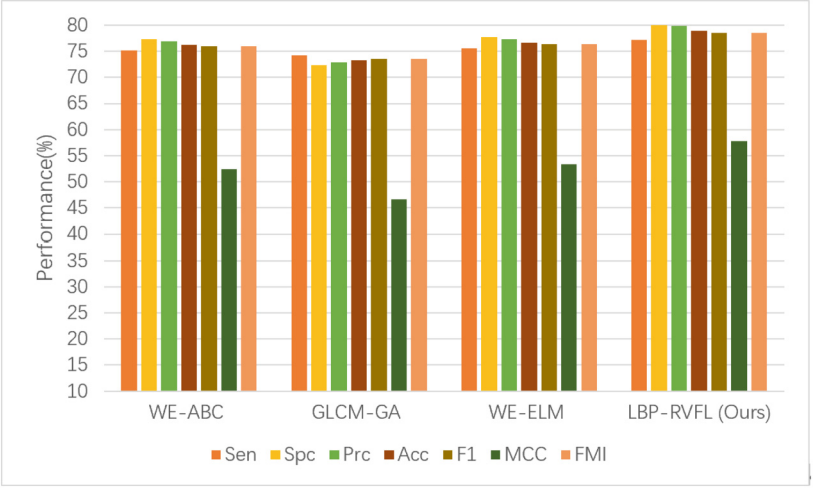

Fig. 13. Bar plot of comparison results.

5 Conclusion

The thesis proposes a hybrid network model for detecting Covid-19, which uses LBP for feature extraction and then divides the images into those suffering from Covid-19 and healthy images using the RVFL algorithm. The model proposes a non-contact diagnostic system. It has fast and accurate characteristics. It has been experimentally proven to be used for Covid-19 diagnosis and to help doctors screen patients. The experiment investigated the ability of RVFL to predict Covid-19 outbreaks. However, limitations of the study were identified. For example, RVFL currently indicates a single sample category, using only time series data samples. In future research, attempts could be made to include more sample categories. In this way, we can re-center better data and significantly improve the model's predictive performance.

Finally, we evaluated the model's sensitivity, specificity, precision, accuracy, F1, MCC, and FMI. The average values were $77.22 \pm 2.33\%$, $80.53 \pm 1.68\%$, $79.89 \pm 1.08\%$, $78.88 \pm 0.79\%$, $78.51 \pm 1.06\%$, $57.82 \pm 1.54\%$ and $78.53 \pm 1.03\%$. The results showed that the model has good sensitivity, accuracy, and precision and can be well used to classify Covid-19.

References

1. Sigalas, C.: Impact of COVID-19 lockdowns on retail stock trading patterns. Cogent Econ. Finance **11**(1), Article no. 2188713 (2023)
2. Hanauer, C., Telaar, B., Al-Dawaf, N., Rosner, R., Doering, B.K.: 'Feeling disconnected' - risk factors for PGD and themes in grief counselling during the COVID-19 pandemic. A mixed-method study. Eur. J. Psychotraumatol. **14**(1), Article no. 2183006 (2023)
3. Attallah, O.: RADIC: a tool for diagnosing COVID-19 from chest CT and X-ray scans using deep learning and quad-radiomics. Chemometr. Intell. Lab. Syst. **233**, 104750 (2023)
4. Tuncer, T., Dogan, S., Ozyurt, F.: An automated residual exemplar local binary pattern and iterative ReliefF based COVID-19 detection method using chest X-ray image. Chemometr. Intell. Lab. Syst. **203**, 104054 (2020)
5. Zhang, Y., Khan, M.A.: SNELM: squeezeNet-guided ELM for COVID-19 recognition. Comput. Syst. Sci. Eng. **46**(1), 13–26 (2023)
6. Wang, S.-H., Khan, M.A.: WACPN: a neural network for pneumonia diagnosis. Comput. Syst. Sci. Eng. **45**(1), 21–34 (2023)
7. Elemam, N.M., Talaat, I.M., Maghazachi, A.A., Saber-Ayad, M.: Liver injury associated with COVID-19 infection: pathogenesis, histopathology, prognosis, and treatment. J. Clin. Med. **12**, Article no. 2067 (2023)
8. Al Kaabi, N., et al.: Efficacy and safety of a booster vaccination with two inactivated SARS-CoV-2 vaccines on symptomatic COVID-19 infection in adults: results of a double-blind, randomized, placebo-controlled, phase 3 trial in Abu Dhabi. Vaccines **11**(2), Article no. 299 (2023)
9. Zhang, Y.-D.: A five-layer deep convolutional neural network with stochastic pooling for chest CT-based COVID-19 diagnosis. Mach. Vis. Appl. **32**, Article no. 14 (2021)
10. Wang, S.-H., Fernandes, S.: AVNC: attention-based VGG-style network for COVID-19 diagnosis by CBAM. IEEE Sens. J. **22**(18), 17431–17438 (2022)
11. Zhang, Y.D., Satapathy, S.: A seven-layer convolutional neural network for chest CT-based COVID-19 diagnosis using stochastic pooling. IEEE Sens. J. **22**(18), 17573–17582 (2022)

12. Sadik, F., Dastider, A.G., Subah, M.R., Mahmud, T., Fattah, S.A.: A dual-stage deep convolutional neural network for automatic diagnosis of COVID-19 and pneumonia from chest CT images. Comput. Biol. Med. **149**, 105806 (2022)
13. Wang, J., Wang, S., Zhang, Y.: Artificial intelligence for visually impaired. Displays **77** (2023)
14. Alghamdi, M.M.M., Dahab, M.Y.H., Alazwary, N.H.A.: Enhancing deep learning techniques for the diagnosis of the novel coronavirus (COVID-19) using X-ray images. Cogent Eng. **10**(1), Article no. 2181917 (2023)
15. Wang, S.-H.: COVID-19 classification by CCSHNet with deep fusion using transfer learning and discriminant correlation analysis. Inf. Fus. **68**, 131–148 (2021)
16. Farrokh, M., Fallah, M.R.: Flutter instability boundary determination of composite wings using adaptive support vector machines and optimization. J. Braz. Soc. Mech. Sci. Eng. **45**(3), Article no. 181 (2023)
17. Ismael, A.M., Sengur, A.: Deep learning approaches for COVID-19 detection based on chest X-ray images. Expert Syst. Appl. **164**, 114054 (2021)
18. Jain, R., Gupta, M., Taneja, S., Hemanth, D.J.: Deep learning based detection and analysis of COVID-19 on chest X-ray images. Appl. Intell. **51**(3), 1690–1700 (2021)
19. Aminu, M., Ahmad, N.A., Noor, M.H.M.: Covid-19 detection via deep neural network and occlusion sensitivity maps. Alex. Eng. J. **60**(5), 4829–4855 (2021). (in English)
20. Zhang, X., Tang, C., Zhang, Y.-D., Wu, X., Wang, S.-H.: Diagnosis of COVID-19 by Wavelet Renyi entropy and three-segment biogeography-based optimization. Int. J. Comput. Intell. Syst. **13**(1) (2020)
21. Khan, S.H., Sohail, A., Zafar, M.M., Khan, A.: Coronavirus disease analysis using chest X-ray images and a novel deep convolutional neural network. Photodiagnosis Photodyn. Ther. **35**, 102473 (2021)
22. Srivastava, G., Pradhan, N., Saini, Y.: Ensemble of deep neural networks based on Condorcet's Jury theorem for screening Covid-19 and pneumonia from radiograph images. Comput. Biol. Med. **149**, 105979 (2022)
23. Jiang, X., Brown, M., Hu, Z., Cheong, H.-R.: Covid-19 diagnosis by Gray-level cooccurrence matrix and genetic algorithm. EAI Endorsed Trans. e-Learn. **8**(1) (2022)
24. Han, X., Hu, Z., Wang, W.: COVID-19 diagnosis by wavelet entropy and extreme learning machine. EAI Endorsed Trans. e-Learn. **8**(1) (2022)
25. Dammu, H., Ren, T.M., Duong, T.Q.: Deep learning prediction of pathological complete response, residual cancer burden, and progression-free survival in breast cancer patients. PLoS ONE **18**(1), Article no. e0280148 (2023)
26. Ahmed, A., Mohammad, Y.F.O., Parque, V., El-Hussieny, H., Ahmed, S.: End-to-end mobile robot navigation using a residual deep reinforcement learning in dynamic human environments. In: 18th IEEE/ASME International Conference on Mechatronic and Embedded Systems and Applications (MESA), Taipei, Taiwan. IEEE (2022)
27. Negi, A., Kumar, K.: End-to-end residual learning-based deep neural network model deployment for human activity recognition. Int. J. Multimedia Inf. Retr. **12**(1), Article no. 1 (2023)
28. Ghosh, S.K., Ghosh, A.: ENResNet: a novel residual neural network for chest X-ray enhancement based COVID-19 detection. Biomed. Signal Process. Control **72**, 103286 (2022)
29. Tran, V.T., Nguyen, B.P., Doan, N.P., Tran, T.D.: Performance of different CNN-based models on classification of steel sheet surface defects. J. Eng. Sci. Technol. **18**(1), 554–562 (2023)
30. Li, D., Shen, Y., Kong, F.Q. , Liu, J.H., Wang, Q.: Spectral-spatial prototype learning-based nearest neighbor classifier for hyperspectral images. IEEE Trans. Geosci. Remote Sens. **61**, Article no. 5502215 (2023)
31. Maheshwari, S., Sharma, R.R., Kumar, M.: LBP-based information assisted intelligent system for COVID-19 identification. Comput. Biol. Med. **134**, 104453 (2021)

32. Salau, H.O., Abisoye, O.A., Oyefolahan, I.O., Adepoju, S.A.: Enhanced chest X-ray classification model for Covid-19 patients using HOG and LBP. Presented at the 2022 5th Information Technology for Education and Development (ITED) (2022)
33. Ojala, T., Pietikainen, M., Maenpaa, T.: Multiresolution grayscale and rotation invariant texture classification with local binary patterns. IEEE Trans. Pattern Anal. Mach. Intell. **24**(7), 971–987 (2002)
34. Zhang, P.B., Yang, Z.X.: A new learning paradigm for random vector functional-link network: RVFL. Neural Netw. **122**, 94–105 (2020)
35. Souiyah, M.: Elemental compositional modeling of magnetic ordering temperature for spinel ferrite magnetocaloric compounds using intelligent algorithms. Cogent Eng. **10**(1), Article no. 2172790 (2023)
36. Arias-Rodriguez, L.F., Tuzun, U.F., Duan, Z., Huang, J.S., Tuo, Y., Disse, M.: Global water quality of inland waters with harmonized landsat-8 and sentinel-2 using cloud-computed machine learning. Remote Sens. **15**(5), Article no. 1390 (2023)
37. Sharma, R., Goel, T., Tanveer, M., Dwivedi, S., Murugan, R.: FAF-DRVFL: fuzzy activation function based deep random vector functional links network for early diagnosis of Alzheimer disease. Appl. Soft Comput. **106** (2021)
38. Yang, L.: EDNC: ensemble deep neural network for Covid-19 recognition. Tomography **8**(2), 869–890 (2022)
39. Shi, J., et al.: Cascaded multi-column RVFL+ classifier for single-modal neuroimaging-based diagnosis of Parkinson's disease. IEEE Trans. Biomed. Eng. **66**(8), 2362–2371 (2019)
40. Sahoo, J.P., Sahoo, S.P., Ari, S., Patra, S.K.: DeReFNet: dual-stream dense residual fusion network for static hand gesture recognition. Displays **296**, Article no. 102388 (2023)
41. Ali, S.I., et al.: Prediction of asphaltene stability in crude oils using machine learning algorithms. Chemometr. Intell. Lab. Syst. **235**, Article no. 104784 (2023)
42. Zhang, Y.D., Satapathy, S.C.: Fruit category classification by fractional Fourier entropy with rotation angle vector grid and stacked sparse autoencoder. Expert Syst. **39**(3) (2022)
43. Li, B.: Hearing loss classification via AlexNet and extreme learning machine. Int. J. Cognit. Comput. Eng. **2**, 144–153 (2021)
44. Düntsch, I., Gediga, G.: Indices for rough set approximation and the application to confusion matrices. Int. J. Approx. Reasoning **118**, 155–172 (2020)
45. Zhang, Y.D., et al.: Advances in multimodal data fusion in neuroimaging: overview, challenges, and novel orientation. Inf. Fus. **64**, 149–187 (2020)
46. Khan, A., et al.: Computer-assisted diagnosis of lymph node metastases in colorectal cancers using transfer learning with an ensemble model. Mod. Pathol. **36**(5), Article no. 100118 (2023)
47. Mills, S.A., Bousiotis, D., Maya-Manzano, J.M. , Tummon, F., MacKenzie, A.R., Pope, F.D.: Constructing a pollen proxy from low-cost optical particle counter (OPC) data processed with neural networks and Random Forests. Sci. Total Environ. **871**, Article no. 161969 (2023)
48. Hachaj, T., Mazurek, P.: Comparative analysis of supervised and unsupervised approaches applied to large-scale "in the wild" face verification. Symmetry **12**(11) (2020)